



Full paper

Vertically rooting multifunctional tentacles on carbon scaffold as efficient polysulfide barrier toward superior lithium-sulfur batteries

Junfan Zhang^{a,1}, Gaoran Li^{b,1}, Yongguang Zhang^{a,**}, Wen Zhang^a, Xin Wang^c, Yan Zhao^a, Jingde Li^{d,***}, Zhongwei Chen^{b,*}

^a School of Materials Science and Engineering, Tianjin Key Laboratory of Materials Laminating Fabrication and Interface Control Technology, Hebei University of Technology, Tianjin, 300130, China

^b Department of Chemical Engineering, University of Waterloo, Waterloo, ON, N2L 3G1, Canada

^c International Academy of Optoelectronics at Zhaoqing, South China Normal University, Guangdong, China

^d Hebei Provincial Key Laboratory of Green Chemical Technology and High Efficient Energy Saving, School of Chemical Engineering and Technology, Hebei University of Technology, Tianjin, 300130, China

ARTICLE INFO

Keywords:

Interlayer
Lithium sulfur batteries
CNF
Metal-organic framework

ABSTRACT

The rational design of sulfur barrier/host materials plays essential roles in developing high-performance lithium-sulfur (Li-S) batteries. Herein, we developed a hierarchically fibrous framework to establish a conductive, adsorptive, and catalytic barrier toward inhibition on polysulfide shuttling and enhancement in Li-S battery performance. The weaving carbonaceous scaffold with vertically-rooted carbon nanofiber (CNF) tentacles facilitates both short- and long-range electrical conduction as well as efficient exposure of active sites, while the multiple adsorptive and catalytic sites enable strong sulfur confinement and expedited sulfur conversion, thus contributing to a fast and durable sulfur electrochemistry. Attributed to these favorable features, Li-S cells based on the as-developed interlayer achieve excellent cyclability with minimum capacity fading rate of 0.018% over 1000 cycles, high rate capability up to 3 C, and decent performance under high raised sulfur loading up to 8 mg cm⁻².

1. Introduction

Lithium-sulfur (Li-S) batteries are highly expected to power the next-generation of energy storage due to the low-cost of sulfur, high theoretical specific capacity (1675 mAh g⁻¹), and high energy density (2600 Wh kg⁻¹) [1–3]. However, their practical application is challenged by the low electronic conductivity of sulfur, large volume variation upon charge-discharge, and most importantly the rapid capacity degradation caused by the dissolution and migration of the intermediate lithium polysulfides (LiPS) [4–6]. These polysulfide behaviors are usually referred to the so-called “shuttle effect”, representing the major obstacle in the development of high-performance Li-S batteries [7,8].

During the past few decades, extensive research efforts including the various structural designs of sulfur cathode and functional interlayers, have been devoted to tackling the above-mentioned problems [9–12].

The rationale behind these strategies lies in the construction of hosting or barrier materials that can physically/chemically confine LiPS for the inhibition of shuttle effect. Until now, heteroatom-doped (such as N, S and P) carbon materials and their composites with polar metal oxides/sulfides have been demonstrated to chemically trapping LiPS for sulfur immobilization [13–15]. Additionally, these carbon-based materials are intentionally constructed with considerable porosities to physically accommodate and confine LiPS. Such combination of physical and chemical polysulfide adsorptions had shown great capability of stabilizing the sulfur electrochemistry and enhancing the energy efficiency of Li-S batteries. Beyond that, studies have reported that blocking the LiPS diffusion offers promising solution to the shuttling issue when it combines good adsorptive and electrocatalytic features [16–18]. The cooperative fulfillments of strong LiPS confinement and fast LiPS conversions are expected to well restrain the active sulfur species within the cathodic section and suppress the polysulfide shuttling behaviors,

* Corresponding author.

** Corresponding author.

*** Corresponding author.

E-mail addresses: yongguangzhang@hebut.edu.cn (Y. Zhang), jingdeli@hebut.edu.cn (J. Li), zhwchen@uwaterloo.ca (Z. Chen).

¹ The authors contributed equally to this work.

thus contributing to a fast and reversible sulfur redox chemistry. However, the establishment of highly effective LiPS barrier complying this concept is still challenging and calls for rational designs at material level.

In this contribution, we developed an elaborate interlayer architecture with hierarchically fibrous conductive network and multiple adsorptive/catalytic sites for the establishment of reliable polysulfide barrier and the improvement of Li-S battery performance. The interlayer material was prepared through a facile CVD process with the Ni-etched zeolitic imidazole framework-67 (ZIF-67) serving concurrently as metal and auxiliary gas sources. The obtained interlayer delivers a hierarchical fibrous structure with carbon nanofiber (CNF) tentacles vertically rooted on the self-standing carbon fabric (CF) matrix, which ensures both short- and long-range electrical conduction as well as efficient exposure of active sites for sulfur redox reactions. Meanwhile, the pyrolysis of ZIF endows the interlayer with abundant N doping, M (Co, Ni)-N-C heterostructure, and ultrafine metal particles, which sever as multiple adsorptive and electrocatalytic sites for efficient sulfur immobilization and conversion [19]. Attributed to these favorable features, the obtained interlayer builds a reliable barrier that captures and reutilizes LiPS against their diffusion across the separator, thus contributing to significant inhibition on polysulfide shuttling and enhancement in battery performance. The Li-S cells based on the as-developed interlayer achieves excellent cyclicality with a high capacity retention of 82.4% after 1000 cycles, superb rate capability up to 3C, and high areal capacity of 7.04 mAh cm⁻² under raised sulfur loading, clearly demonstrating the superiorities of such interlayer design in favoring fast and durable sulfur electrochemistry.

2. Experimental

2.1. Synthesis of ZIF67@CF and NiCo-LDH@CF

Typically, 249.0 mg (1 mmol) of cobalt nitrate hexahydrate [Co(NO₃)₂·6H₂O] and 328.0 mg (4 mmol) of 2-methylimidazole were dissolved in 25 mL methanol, respectively. The two solutions were then mixed quickly under vigorous stirring. After that, carbon fabric (CF) was immersed into the mixed solution, and aged for 24 h at room temperature. The product (denoted as ZIF67@CF) was collected, washed with methanol and dried naturally. The NiCo-LDH@CF was prepared by etching the as-obtained ZIF67@CF in a solution containing 90 mg nickel nitrate in 25 ml ethanol under stirring for 1 h.

2.2. Synthesis of Co-CNF@CF and NiCo-CNF@CF

The synthesis of Co-CNF@CF and NiCo-CNF@CF were performed through a CVD process. Typically, the as-prepared ZIF67@CF was heated to 550 °C in Ar atmosphere with a ramping rate of 2 °C min⁻¹, followed by switching the Ar gas to C₂H₂/H₂ (95:5 in volume ratio) and maintaining at 550 °C for 30 min. After that, the gas was switched back to Ar and naturally cooled down to yield Co-CNF@CF. NiCo-CNF@CF was obtained through the same procedures but with NiCo-ZIF@CF as precursor. The thickness of the final product NiCo-CNF@CF was around 40 μm with an areal density of 1.3 mg cm⁻².

2.3. Material characterization

Powder X-ray diffraction (D8 Focus, Bruker, Germany) using Cu-Kα radiation was employed to investigate the crystalline phase in the as-developed samples. Scanning electron microscopy (SEM) micrographs were collected on a Hitachi, S-4800 microscope. Transmission electron microscopy (TEM) was performed on a JEM2100F, JEOL microscope. Raman spectra were obtained with a micro-Raman spectrometer (LabRAM, HR Evolution). X-ray photoelectron spectra (XPS) were recorded by a Thermal Fisher Scientific ESCALAB 250Xi spectrometer to analyze the chemical states of the interlayer surface. The specific

surface areas of the samples were calculated by the Brunauer-Emmett-Teller (BET) equation according to the N₂ adsorption-desorption isotherms measured by a V-Sorb 2800P analyzer. The UV-Vis spectra was obtained in the 250–800 nm spectral range using a Cary 60 UV-Vis spectrophotometer.

2.4. Electrochemical measurements

The sulfur@reduced graphene oxide (S@rGO) composite was used as the cathode active material, which was prepared via a melting-diffusion method. The rGO was obtained through the hydrothermal reduction of graphene oxide followed by a freeze-drying process. The S@rGO electrodes were fabricated by coating the slurry containing S@rGO, Super P, and polyvinylidene fluoride (PVDF) binder in mass ratio of 8:1:1 in N-Methyl-2-pyrrolidone (NMP) on Al foil. The areal sulfur loading was around 2.1 mg cm⁻². The electrodes were cut into wafers in diameter of 12 mm for cell assembly. The CR2025-type coin cells were assembled in a glove box (H₂O and O₂ < 0.5 ppm) with lithium foil and Celgard as anode and separator, respectively. The electrolyte contains 1.0 M lithium bis (trifluoromethane sulfonate) imide in binary solvent of 1,3-dioxolane (DOL) and 1,2-dimethoxyethane (DME) (1:1 in volume) with 0.1 M LiNO₃ as additive. The electrolyte addition was 40 μL for each cell. Galvanostatic cycling was performed on a multi-channel battery tester (BTS-5V5mA, Neware) within a cut-off voltage window of 1.7 V–2.8 V at room temperature. Cyclic voltammetry (CV) and electrochemical impedance spectroscopy (EIS) were recorded on electrochemical workstation (Princeton, Versa STAT 4).

2.5. Density functional theory calculations

DFT calculations were performed using the Vienna Ab initio Simulation Package (VASP) program. The electron-ion interaction and exchange-correlation energy were described using projected augmented wave potential and generalized gradient approximation with the Perdew-Burke-Ernzerhof (PBE) functional, respectively. A plane-wave cut off energy of 400 eV was applied. The k-space was sampled using a 2 × 2 × 1 Monkhorst-Pack grid. A vacuum height of 15 Å was used between successive slabs. Li₂S₆ was employed as representative of LiPS. The Ni and Co nanoparticles were modeled on (111) surface as it is the main crystal orientation as revealed by XRD and HRTEM. Meanwhile, the LiPS adsorption on pyrrolic N was studied because it is the main state observed in XPS analysis. In all the calculations, the ground-state atomic geometries were fully relaxed by minimizing the forces on the atoms smaller than 0.03 eV/Å. The binding energies (*E_b*) between Li₂S₆ and the adsorptive sites are defined as follows:

$$E_b = E_{Li_2S_6/slab} - E_{slab} - E_{Li_2S_6}$$

where *E_{Li₂S₆/slab}* represents the total energy of adsorbed system, *E_{slab}* is the energy of a clean relaxed Ni/Co or NC slab, *E_{Li₂S₆}* is the energy of isolated Li₂S₆. A more negative *E_{ads}* indicates a stronger interaction with Li₂S₆.

3. Results and discussion

The synthesis of the interlayer material was schematically illustrated in Fig. 1. The basic idea of this scenario lies in the combination of doping chemistry and hierarchical architecture to achieve a multi-functional matrix for improved sulfur electrochemistry (Fig. 1a). A lightweight carbon fabric (CF) with areal density of 1.0 mg cm⁻² was employed as the substrate for the construction of desired interlayer functionalities. The pristine CF delivers a crisscrossed fibrous framework with relatively smooth surface as shown in Fig. 2a and Fig. S1, offering a favorable mechanical robustness and 3D long-range conductivity for sulfur electrochemical reactions. After the solution-based MOF growth (see details in Experimental), ZIF67 nano-polyhedrons were tightly and uniformly embedded on the CF surface as shown in

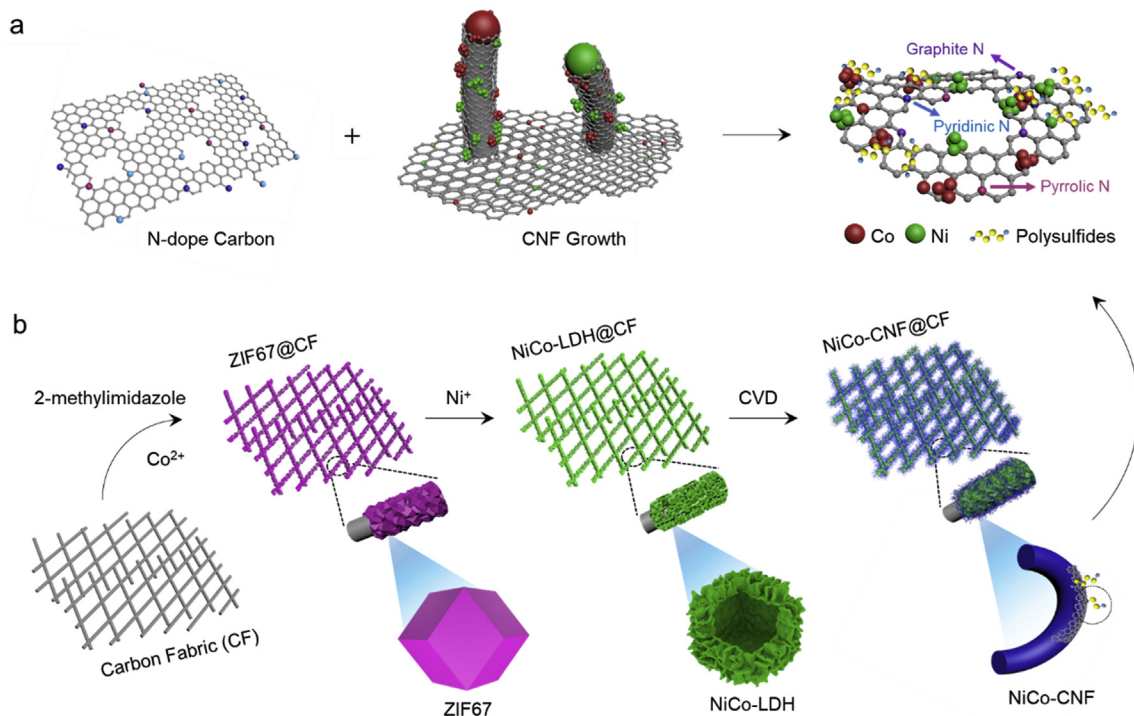


Fig. 1. (a) Designing strategy and (b) schematic illustration for the development of NiCo-CNF@CF interlayer.

Fig. 2b. The successful loading of ZIF67 crystal was also confirmed by XRD patterns (Fig. S2). Upon the Ni-etching, the ZIF67 polyhedrons serve as the sacrificial template and transform into the hollow-structured polyhedral assembly of NiCo-layered double hydroxide (NiCo-

LDH) nanosheets as shown in Fig. 2c [21]. Such transition can be further supported by the obvious color change from ZIF67 to NiCo-LDH, while a small size reduction was perceived as shown in Fig. S3. Subsequently, the obtained NiCo-LDH@CF was performed with a CVD

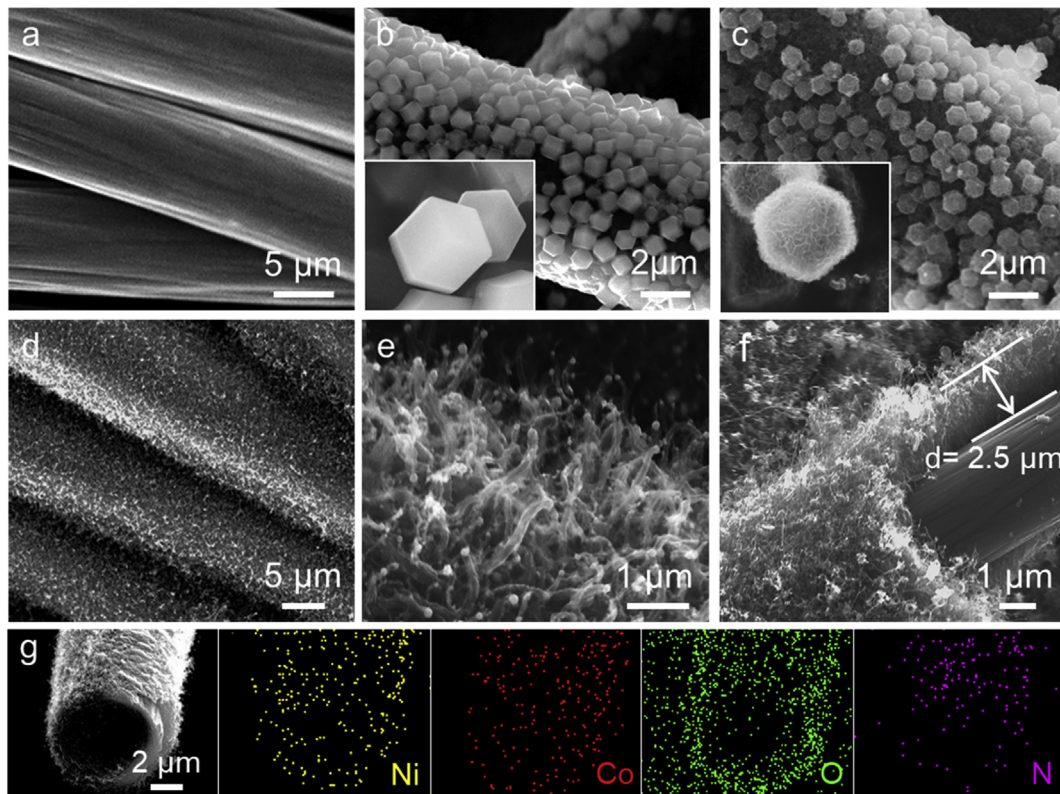


Fig. 2. SEM images of (a) CF, (b) ZIF67@CF, (c) NiCo-LDH@CF, and (d–f) NiCo-CNF@CF; (g) element mapping of NiCo-CNF@CF.

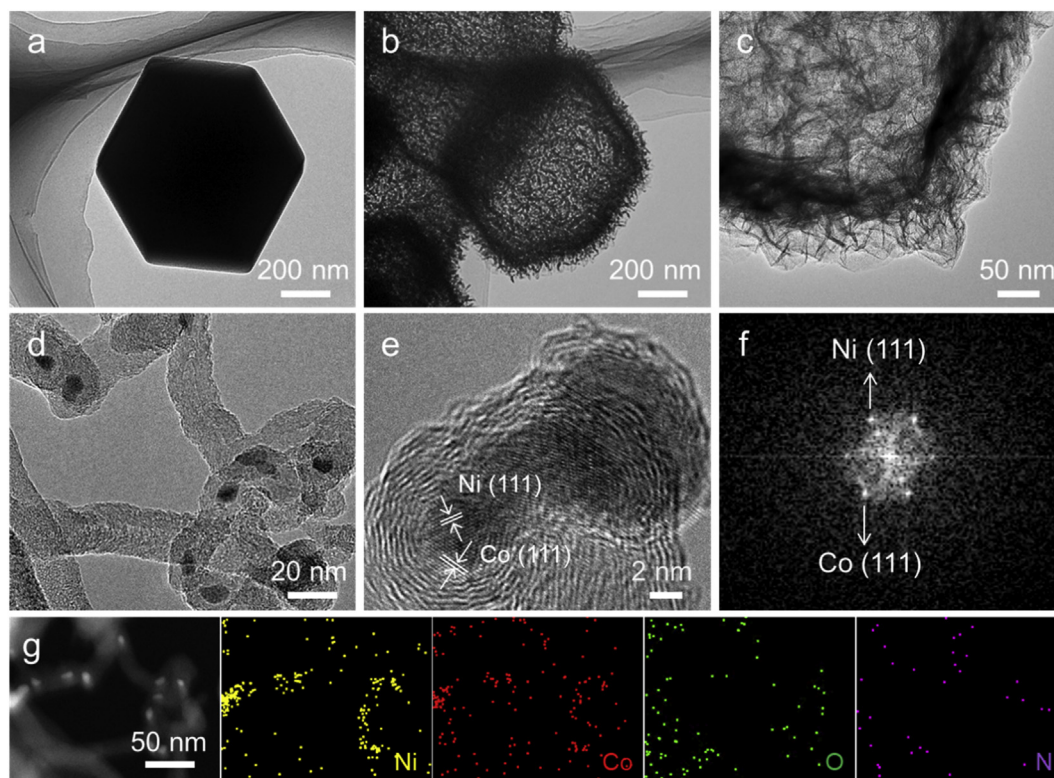


Fig. 3. TEM images of (a) ZIF67, (b, c) NiCo-LDH, (d–e) NiCo-CNF@CF; (f) SAED pattern and (g) element mapping of NiCo-CNF@CF.

process, during which the metal ions were reduced by the reductive atmosphere from the decomposition of Co-ZIF as well as the CVD gas. The as-formed metal nanoparticles in turn catalyze the growth of carbon nanofiber (CNF) sourced by the N-contained decomposition gas and C_2H_2 in CVD gas, rendering the abundant CNF tentacles well aligned on CF fibers as shown in Fig. 2d–f. The CNF are around 20 nm in diameter, while the thickness of CNF layer on CF substrate is around 25 μm . The CNF tentacles are expected to offer good short-range electron conduction for sulfur redox reactions, and meanwhile constructing higher porosity for physical sulfur confinement. The element mapping confirms the uniform distribution of Ni, Co, O and N, which also implies the heteroatom N doping and partial oxidation in the obtained NiCo-CNF@CF (Fig. 2g). The morphological evolution was further investigated by TEM observations. As shown in Fig. 3a–c, the ZIF67 crystal shows a solid polyhedral structure, while the Ni-etching converts it into the hollow polyhedrons assembled by plentiful thin nanosheets. Subsequently, the CVD process cultivates numerous N-doped CNF embedded with ultrafine Ni and Co particles as confirmed by the interplanar spacing, selected area electron diffraction (SAED) pattern and element mapping (Fig. 3d–g).

XRD measurements were conducted to further investigate the composition of the products. As shown in Fig. 4a, a strong peak at around 25° can be observed for both NiCo-LDH@CF and NiCo-CNF@CF, which is assigned to the (002) reflection of graphitic carbon [20]. Additionally, NiCo-LDH@CF exhibits a small peak at $\sim 12^\circ$ ascribed to the (003) lattice plane of NiCo-LDH, confirming the formation of LDH nanocrystal after the Ni-etching [21]. By contrast, this LDH diffraction peak disappears in NiCo-CNF@CF pattern while new peaks emerge at around 44° , manifesting the decomposition and conversion of NiCo-LDH into metallic Co and Ni (PDF#89–7093 and 70–0989, respectively) [22,23]. Moreover, the porous characters of NiCo-LDH@CF and NiCo-CNF@CF were studied by N_2 adsorption-desorption. The isotherms show a stronger adsorptive behavior of NiCo-CNF@CF than that of NiCo-LDH@CF, indicating the considerable porosity enhancement after CVD process (Fig. 4b). This is also supported by the higher

specific surface area of NiCo-CNF@CF ($95.7 \text{ m}^2 \text{ g}^{-1}$) than that of NiCo-LDH@CF ($34.1 \text{ m}^2 \text{ g}^{-1}$). The pore distribution reveals that the primary enhancement lies in the microporous range (Fig. 4c), which is expected to strengthen the physical sulfur confinement toward inhibition on polysulfide shuttling. The higher surface area also favors the efficient exposure of active sites as well as offering abundant electrode/electrolyte interfaces for sulfur conversion reactions. Apart from that, the porosity of ZIF67@CF and Co-CNF@CF were also investigated as shown in Fig. S4. As the ZIF67 delivers an intrinsic microporosity, the CVD treatment also constructs considerable CNF on the obtained Co-CNF@CF (Fig. S5), and meanwhile endowing it with increased mesoporous structures. Given this, the Ni-etching is comprehended to introduce Ni species into the substrate and simultaneously drive the metal species towards the surface, which enhances the intrinsic catalytic activity and the catalytic exposure respectively for a more efficient CVD process [24]. The porous structure parameters of different interlayer materials are summarized in Table S1). Therefore, the as-developed NiCo-CNF@CF delivers luxuriant CNF arrays with higher porosity and larger surface area than those of Co-CNF@CF obtained by sole Co-based CVD. Beyond that, both Ni and Co are expected to establish adsorptive and catalytic sites to favor fast and stabilized sulfur electrochemistry, which will be discussed in later sections.

The surface chemistry of the as-developed NiCo-CNF@CF was investigated by X-ray photoelectron spectroscopy (XPS) analysis. The XPS survey confirms the existence of Ni, Co, O and N in NiCo-CNF@CF (Fig. S6), which is consistent with the element mapping results. The element contents were listed in Table S2. The C 1s spectrum confirms the heteroatom N doping in the carbon lattice by showing the C=N and C-N bonding at 285.8 and 288.5 eV, respectively (Fig. S6b) [25]. The high-resolution Ni 2p spectrum can be deconvoluted into several sub peaks assigned to Ni^0 , Ni^{2+} , and satellite as shown in Fig. 4d [26]. Meanwhile, the Co 2p spectrum also exhibits the multiple valence states of Co in Co^0 , Co^{3+} and Co^{2+} (Fig. 4e) [27]. These results confirm the existences metallic Ni and Co in NiCo-CNF@CF in line with the TEM observations, as well as their partial oxidation on surface. The chemical

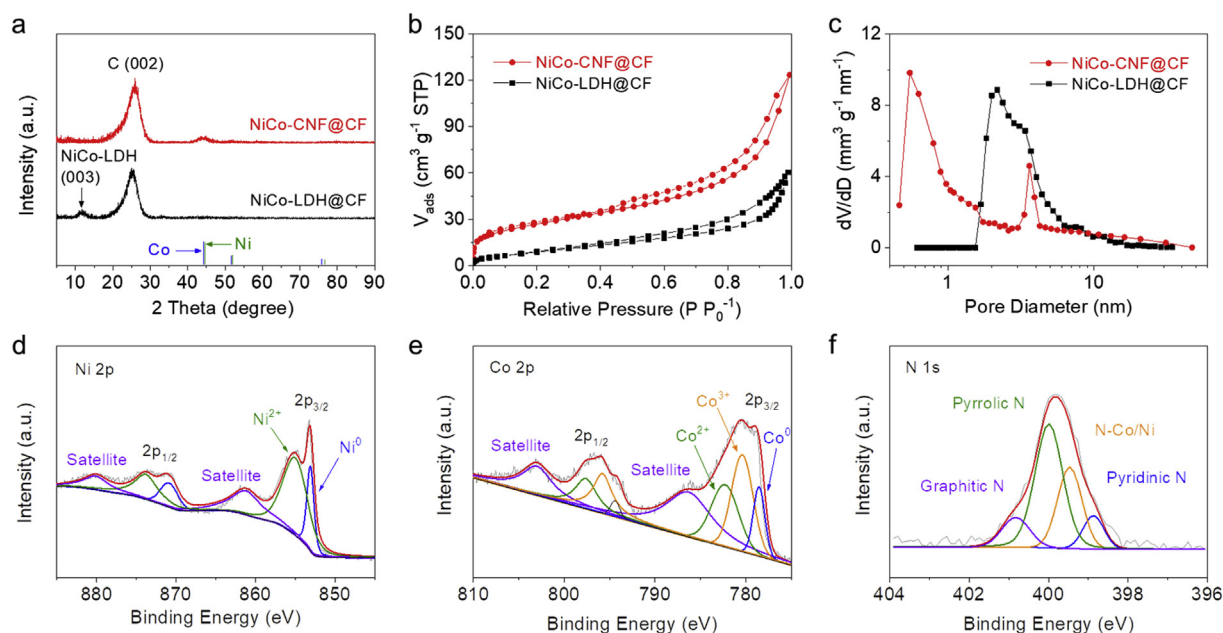


Fig. 4. (a) XRD patterns, (b) isotherms and (c) pore distribution of NiCo-LDH@CF and NiCo-CNF@CF; (d) Ni 2p, (e) Co 2p and (f) N 1s spectra of NiCo-CNF@CF.

states of N are revealed in N 1s spectrum in Fig. 4f, which can be differentiated into four sub-peaks corresponding to pyridinic N, N-Co/Ni bonding, pyrrolic N and graphitic N, respectively, suggesting the formation of M-N-C coordination [28]. The M-N-C coordination has been extensively studied as the active sites for oxygen redox catalysis, which is also expected to catalyze the sulfur redox reactions in view of the considerable similarities between sulfur and oxygen electrochemistries [29,30]. Furthermore, the N-doping also endows the carbonaceous skeleton with higher polar lattice and the resultant higher affinity to LiPS, while the metallic nanoparticles, metal oxides and the M-N-C structures could also serve as multiple adsorptive sites to chemically confine sulfur species and catalyzing the sulfur conversions toward fast and durable sulfur electrochemistry.

The electrochemical evaluations were performed in coin-cell configuration by using S/rGO as cathode active materials. The S/rGO composite was prepared via conventional melting-diffusion method (see details in Experimental) with a sulfur content of ~71 wt% as determined by TGA (Fig. S7). The SEM image and element mapping demonstrate the uniform sulfur distribution in the obtained composite (Fig. S8). Fig. 5a shows the CV curves of Li-S cell with NiCo-CNF@CF interlayer at initial cycles. Two cathodic peaks can be observed at 2.30 and 2.02 (vs. Li⁺/Li, hereinafter inclusive) corresponding to the electrochemical reductions of element sulfur to high-ordered soluble Li₂S_x (4 ≤ x ≤ 8) and further into low-ordered insoluble Li₂S₂/Li₂S, respectively, while the anodic scanning reveals an overlapped peak at around 2.38 V ascribed to the oxidation of sulfur species. It is worth noting that the CV profiles well overlapped upon the initial cycles, signifying the good electrochemical reversibility of Li-S cells based on NiCo-CNF@CF interlayer. The CV curves of cells with Co-CNF@CF, NiCo-LDH@CF and ZIF67@CF modified separators are also presented in Fig. S9, which show similar profiles but with smaller peak densities and larger peak potential gaps, implying the superior reaction kinetics of NiCo-CNF@CF based cells. Consistently, the voltage profile shows a two-plateau discharge curve and a slope charge curve due to the multi-step sulfur electrochemistry (Fig. 5b). The voltage profile well maintains its shape and plateau potentials over 100 cycles with a stabilized capacity at 1108.9 mAh g⁻¹, suggesting a decent reaction kinetics and cycling stability. The charge-discharge curves of the cell with NiCo-CNF@CF at different current rates were also presented in Fig. 5c, which well maintains the distinct two-plateau profile at raised current rate up

to 3 C despite of the somewhat widening of the potential gap between charge and discharge plateaus. By contrast, cells based on Co-CNF@CF, NiCo-LDH@CF and ZIF67@CF interlayers shows considerably severer electrochemical polarization with larger potential gaps at raised rates (Fig. S10), further indicating the superiority of NiCo-CNF@CF interlayer in facilitating the sulfur redox reactions. Such enhancement in reaction kinetics is embodied by the much superior rate capability of NiCo-CNF@CF-based cell with considerably higher capacity of 625.9 mAh g⁻¹ at a current rate up to 3 C than those of Co-CNF@CF (523.7 mAh g⁻¹), NiCo-LDH@CF (368.3 mAh g⁻¹) and ZIF67@CF (208.3 mAh g⁻¹) as shown in Fig. 5d. The EIS spectra before and after cycling reveal the significantly smaller charge-transfer resistance for the cell with NiCo-CNF@CF interlayer, which accounts for its fast reaction kinetics and good rate capability (Fig. 5e and Fig. S11). The cycling performances for different interlayers were evaluated by galvanostatic cycling at 0.2 C (Fig. 5f). The result shows a much higher cycling stability for NiCo-CNF@CF than other interlayers with a high capacity of 1108.9 mAh g⁻¹ after 100 cycles (967.3 mAh g⁻¹, 819.0 mAh g⁻¹ and 504.9 mAh g⁻¹ for Co-CNF@CF, NiCo-LDH@CF and ZIF67@CF, respectively). Notably, NiCo-CNF@CF also enables a higher coulombic efficiency than other interlayers upon the cycling, suggesting its superior inhibition on polysulfide shuttling. To further explore the cyclability, cells with different interlayers were measured for a long-term cycling as shown in Fig. 5g. An excellent capacity retention of 81.5% over 1000 cycles can be achieved for NiCo-CNF@CF corresponding to a minimum capacity fading rate of 0.018% per cycle, which is significantly higher than those for other interlayers (capacity retention of 62.3%, 49.7% and 30.0% for Co-CNF@CF, NiCo-LDH@CF and ZIF67@CF after 1000 cycles, respectively), further confirming the well-regulated polysulfide shuttling and stabilized sulfur electrochemistry in NiCo-CNF@CF-based configuration.

Additionally, cells without interlayers or with pure CF modified separator were also characterized as shown in Fig. S12 and Fig. S13, respectively, which reveals much poorer rate capability and cyclability than those with the as-developed NiCo-CNF@CF, Co-CNF@CF, NiCo-LDH@CF and ZIF67@CF interlayers, certifying the great benefit for electrochemical improvement by these interlayer construction. Given this, cells with NiCo-CNF@CF were further employed at raised sulfur loadings to pursue higher energy density and practical viability. As shown in Fig. 5h, the as-developed NiCo-CNF@CF interlayer is capable

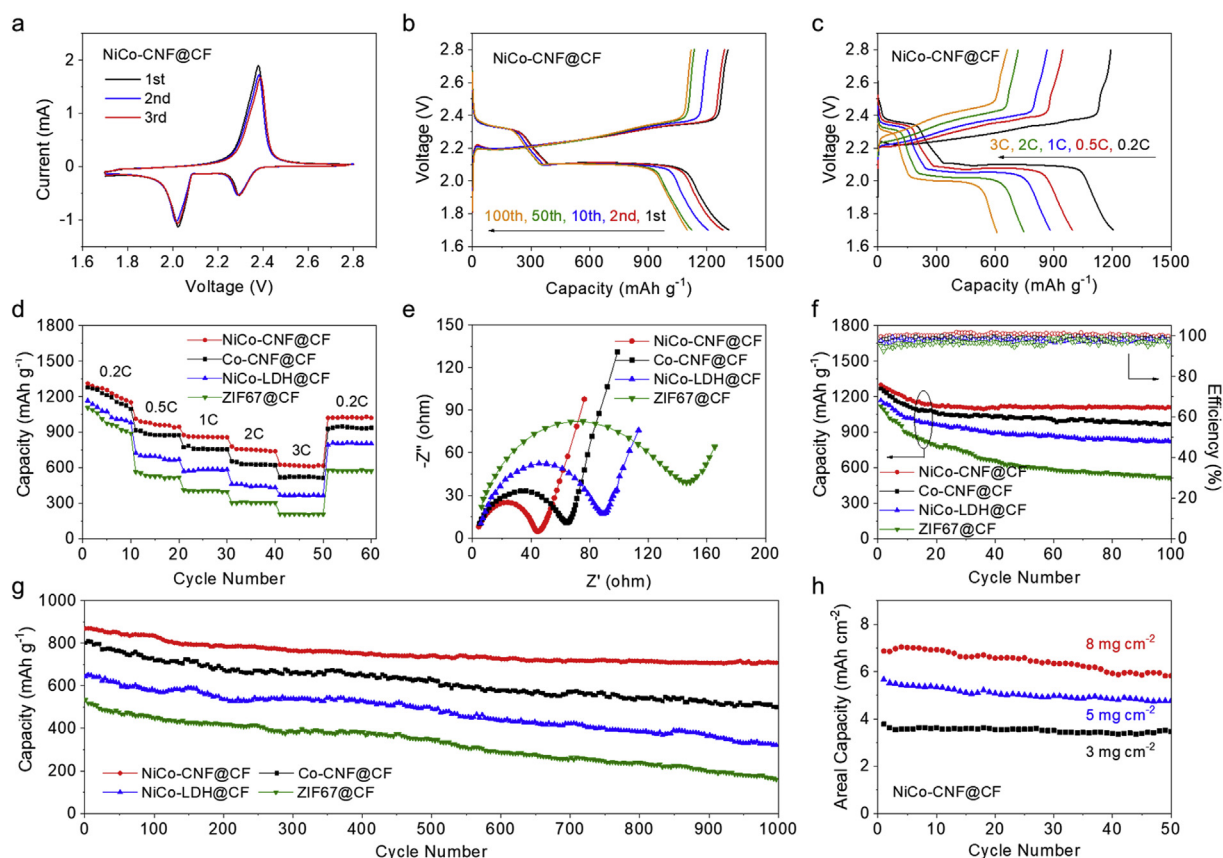


Fig. 5. (a) CV curves, charge-discharge profiles at (b) different cycles and (c) rates; (d) multi-rate cycling, (e) EIS spectra, (f) galvanostatic cycling at 0.2 C and (g) long-term cycling at 1 C performances of Li-S cells with different interlayers; (h) cycling performance of cells with NiCo-CNF@CF interlayer under raised sulfur loadings.

of fulfilling decent sulfur electrochemistry even under a high sulfur loading of 8 mg cm^{-2} with a high areal capacity of 7.04 mAh cm^{-2} and good cycling stability. The charge-discharge curves exhibit the well-maintained two-plateau discharge profiles under raised sulfur loadings, confirming the good reaction kinetics based on this interlayer design (Fig. S14). These results strongly demonstrate the intriguing potential in developing high-energy and practical viable Li-S batteries. It is also noteworthy that the electrochemical performance achieved in the present strategy is highly competitive among the recently published Li-S batteries with interlayer designs, which further confirms the great superiority of the as-developed NiCo-CNF@CF interlayer (Table S3).

In order to understand the underlying mechanism for such improvement in sulfur electrochemistry, an optical observation was performed to investigate the LiPS adsorption behavior. As shown in Fig. 6a, the blank LiPS solution shows a light brown color, while a colorless solution can be achieved after immersing NiCo-CNF@CF for 3 h. The UV-vis spectra also confirm the great decrease of LiPS after adsorption by showing a significantly weakened peak at around 280 cm^{-1} and 415 cm^{-1} , which are referred to the $\text{Li}_2\text{S}_8/\text{Li}_2\text{S}_6$ and Li_2S_4 species, respectively [31]. Moreover, the chemical interactions between LiPS and NiCo-CNF were studied by XPS analysis. As shown in Fig. 6b, the Li spectrum of LiPS shows a peak at 54.9 eV ascribed to the Li-S bonding, while a new peak referring to the Li-N/O bonding emerges at 55.8 eV for NiCo-CNF@CF after the LiPS adsorption, signifying the formation of the “lithium bond”-like configuration [38]. In addition, the S 2p spectrum of LiPS shows two pairs of peaks locating at 161.3 and 162.8 eV ascribed to the terminal sulfur (S_T^{-1}) and bridging sulfur (S_B^0) respectively (Fig. 6c) [32]. After adsorption, a considerable shift of these peaks toward higher binding energy range can be perceived, suggesting a reduction of electron cloud density due to the electron transfer

between LiPS and metal-based species as well as the formation of the N-Li-S configuration [33]. Apart from that, new peak pairs emerge at 166.7 and 168.4 eV in S 2p spectrum after adsorption by NiCo-CNF@CF, which can be ascribed to the formation of thiosulfate and sulfate species respectively [34]. This is likely to originate from the sulfur oxidation by the oxidative species on NiCo-CNF@CF surface, which could favor the chemical sulfur confinement through a sulfur incorporation mechanism [35]. Beyond that, the interactive chemistry between LiPS and active sites in NiCo-CNF@CF was further revealed by computational calculation. As shown in Fig. 7, metallic Ni and Co deliver strong adsorption to Li_2S_6 with a high binding energy of -6.83 and -7.20 eV , respectively. Meanwhile, the “lithium bond” and Lewis base-acid interaction between LiPS and NiCo-CNF@CF can be clearly revealed by the geometrically stable configuration of LiPS on M-N-C and N-C sites with considerable binding energies. Furthermore, SEM and EDS mapping after cycling were characterized as shown in Fig. S15, which reveals a clear sulfur coverage in contrast to the fresh state, further confirming the effective sulfur adsorption as well as conversion reactions on the NiCo-CNF@CF surface. These results cooperatively confirm the strong interactions between LiPS and NiCo-CNF@CF, which serves as chemical trappers for immobilizing the sulfur species and inhibiting their diffusion behaviors across the separator for enhanced sulfur electrochemical reversibility.

For a proof of concept, the diffusion behavior of LiPS was observed in a H-type cell configuration with/without NiCo-CNF@CF interlayer. As shown in Fig. 6d the cell with the conventional Celgard separator undergoes severe LiPS penetration which leads to a dark brown color in the opposite chamber. By contrast, the opposite chamber well maintains a clear and transparent solution when incorporated with NiCo-CNF@CF interlayer, which strongly indicates its great capability of

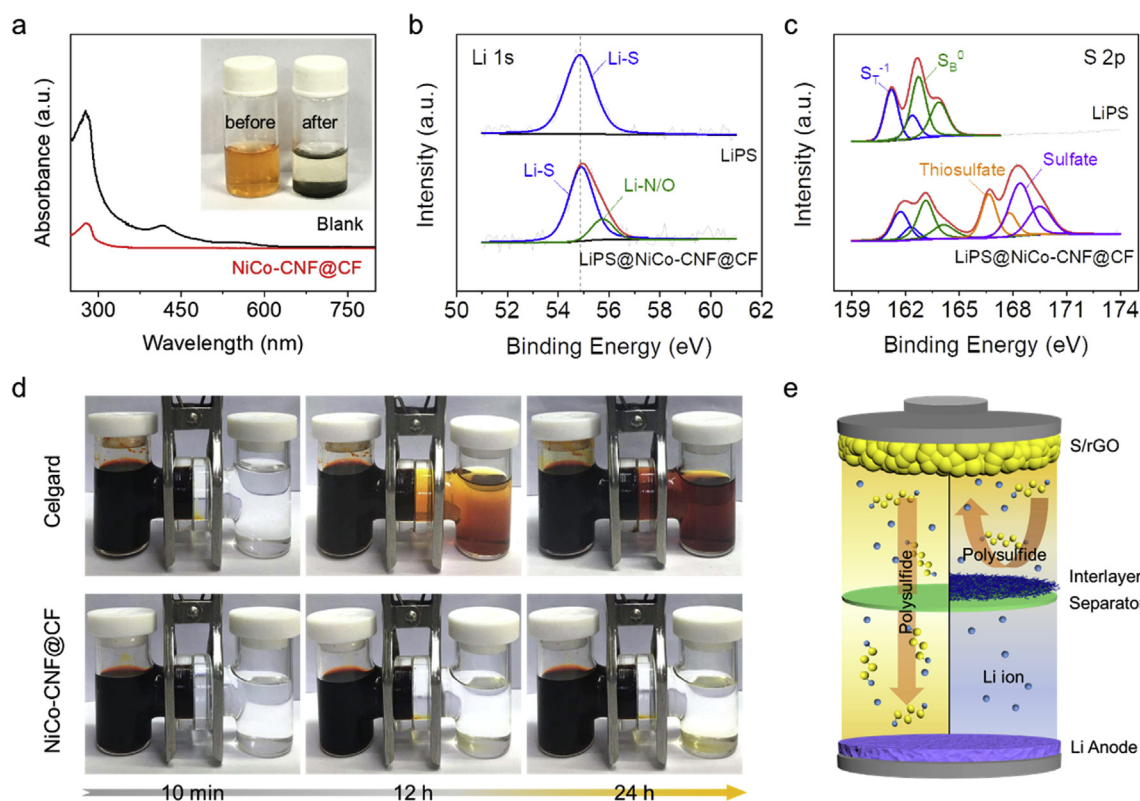


Fig. 6. (a) UV-vis spectra and optical images (inset) of LiPS solution before and after adsorption by NiCo-CNF@CF; (b) Li 1s and (c) S 2p spectra of LiPS and NiCo-CNF@CF after adsorption; (d) optical observation and (e) schematic illustration of LiPS diffusion with or without NiCo-CNF@CF interlayer.

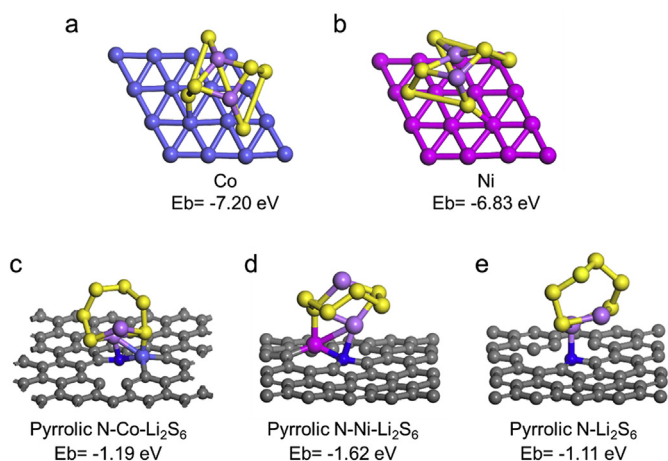


Fig. 7. First-principles calculations illustrating the chemical interactions between LiPS and NiCo-CNF@CF.

confining LiPS and restraining their diffusion across the separator. Benefiting from these attributes, the NiCo-CNF@CF interlayer establishes a reliable barrier that significantly inhibits the shuttle effect, which is schematically illustrated in Fig. 6e, and contributes to the resultant excellent cyclability for the according Li-S batteries.

In addition to LiPS adsorb ability, the sulfur electro-catalysis also plays a great contribution to the improvement of sulfur electrochemistry. As sulfur redox reactions involve the liquid-solid phase conversions of sulfur species, the kinetics could be reflected by the deposition behavior of Li_2S , the conversions behaviors between different soluble LiPS as well as the oxidation of Li_2S to form soluble sulfur species, which are expected to be regulable by varying the interactive chemistry between sulfur species and the substrates [36,37].

Fig. 8a shows the Li_2S deposition profiles on different interlayer surfaces. The depositions were performed by potentiostatic discharge at 2.05 V in LiPS-containing electrolyte with cells previously discharged to 2.06 V to consume most of the high-ordered LiPS. The capacity contributions from the progressive reduction of high-ordered LiPS and the precipitation of Li_2S were mathematically modeled and identified in dark and light colors, respectively [38,39]. Remarkably, cell based on NiCo-CNF@CF exhibits the strongest current response with the highest deposition capacity of 242 mAh g^{-1} (calculated by integral of the current and based on the weight of sulfur in catholyte) than those for other interlayers (190 , 153 and 69 mAh g^{-1} for Co-CNF@CF, NiCo-LDH@CF and ZIF67@CF, respectively), indicating its best capability of promoting the conversion of LiPS into insoluble Li_2S . Apart from that, symmetric cells were also assembled with interlayer materials as identical electrodes in LiPS-containing electrolyte to monitor LiPS conversions. The CV profiles apparently show the largest and sharpest redox peaks with the smallest redox polarization for NiCo-CNF@CF (Fig. 8b), demonstrating its great capability of catalyzing the LiPS conversions attributed to the multiple catalytic designs. The EIS spectra confirm the facile redox reactions on NiCo-CNF@CF surface by showing the smallest electrochemical resistance under the symmetric configuration (Fig. 8c). Beyond that, the sulfide oxidation behavior on different interlayer surfaces was further studied by LSV technique in a three-electrode configuration with $0.1 \text{ M Li}_2\text{S}/\text{methanol}$ and Ag/AgCl electrode as electrolyte and reference, respectively [40]. As shown in Fig. 8d, sulfide oxidation undergoes a sluggish kinetics on glassy carbon with minimum current response even under a relatively large overpotential. Comparatively, the as-prepared interlayer materials exhibit various degrees of kinetic improvement with more sensitive current responses. Among them, NiCo-CNF@CF delivers the smallest onset potential at around -0.45 V and largest oxidation current, evidencing its best effectiveness in lowering the activation energy of the sulfur conversion from solid Li_2S to soluble LiPS. These results together

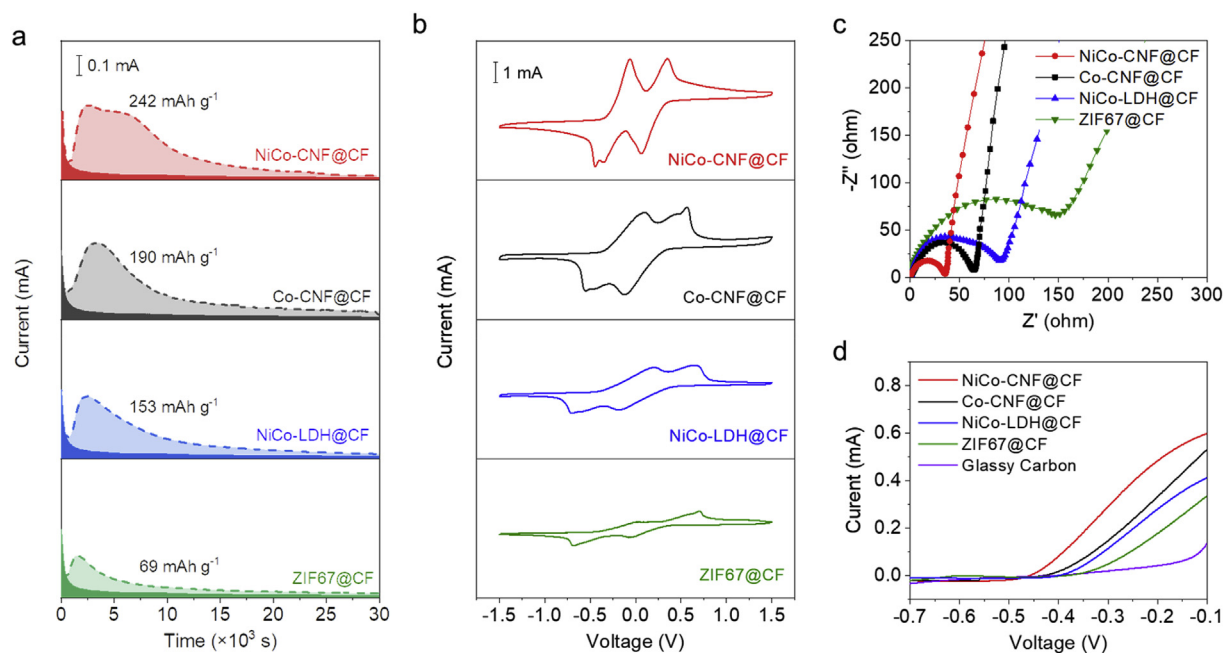


Fig. 8. (a) Li₂S deposition profiles, (b) CV and (c) EIS profiles of symmetric cells, and (d) LSV curves of sulfide oxidation reaction for NiCo-CNF@CF, Co-CNF@CF, NiCo-LDH@CF, and ZIF67@CF.

confirm the significantly catalyzed conversion reactions of sulfur species on the delicately designed NiCo-CNF@CF surface, which enables to the fast and efficient sulfur electrochemistry in the according Li-S configurations.

4. Conclusions

In summary, we have developed a hierarchical fibrous framework with multiple adsorptive/catalytic sites as interlayer for improved Li-S batteries. The carbon fabric aligned with massive CNF tentacles establishes a conductive network favoring both long- and short-range electron transfer, while the high porosity and large surface area contribute to physical sulfur confinement and efficient exposure of active sites. Moreover, the N-doping and metal particles as well as the Ni/Co-N-C coordination serve as multiple adsorptive and catalytic sites that chemically immobilize the LiPS and simultaneously expedite their conversion reactions. Attributed to these superiorities, the as-developed NiCo-CNF@CF interlayer builds a powerful barrier against the polysulfide shuttling, thus leading to fast and reversible sulfur electrochemistry. The according Li-S cell achieved good rate capability up to 3C, excellent cyclability over 1000 cycles, and decent cycling performance under high sulfur loading up to 8 mg cm⁻². This work provides an elaborate interlayer construction towards the mitigation on polysulfide shuttling and enhancement in sulfur redox efficiency, holding a great potential in promoting the development of high-performance of Li-S batteries.

Acknowledgments

This work was supported by the Program for the Outstanding Young Talents of Hebei Province, China; Cultivation Project of National Engineering Technology Center, China (Grant No. 2017B090903008). The authors also thank the financial support from the Natural Sciences and Engineering Research Council of Canada (NSERC), the University of Waterloo, and the Waterloo Institute for Nanotechnology, University of Waterloo.

Appendix A. Supplementary data

Supplementary data to this article can be found online at <https://doi.org/10.1016/j.nanoen.2019.103905>.

References

- [1] H. Pan, J. Chen, R. Cao, V. Murugesan, N.N. Rajput, K.S. Han, K. Persson, L. Estevez, M.H. Engelhard, J.G. Zhang, K.T. Mueller, Y. Cui, Y. Shao, J. Liu, *Nature Energy* 2 (2017) 813–820.
- [2] G.L. Chen, W.T. Zhong, Y.S. Li, Q. Deng, X. Ou, Q.C. Pan, X.W. Wang, X.H. Xiong, C.H. Yang, M.L. Liu, *ACS Appl. Mater. Interfaces* 11 (2019) 5055.
- [3] Y.Y. Zhao, Y.S. Ye, F. Wu, Y.J. Li, L. Li, R.J. Chen, *Adv. Mater.* 31 (2019) 1806532.
- [4] Z.Y. Xing, G.R. Li, S. Sy, Z.W. Chen, *Nano Energy* 54 (2018) 1–4.
- [5] L.X. Song, Z.X. Yu, M.L. Gordin, D.H. Wang, *Nano Lett.* 16 (2016) 864–870.
- [6] W. Ni, J.L. Cheng, X.D. Li, Q. Guan, G.X. Qu, Z.Y. Wang, B. Wang, *RSC Adv.* 6 (2016) 9320–9327.
- [7] Y.C. Jeong, J.H. Kim, S.H. Nam, C.R. Park, S.J. Yang, *Adv. Funct. Mater.* 28 (2018) 1707411.
- [8] Y.J. Li, J.M. Fan, J.H. Zhang, J.F. Yang, R.M. Yuan, J.K. Chang, M.S. Zheng, Q.F. Dong, *ACS Nano* 11 (2017) 11417–11424.
- [9] J.R. He, Y.F. Chen, A. Manthiram, *Energy Environ. Sci.* 11 (2018) 2560.
- [10] Z.P. Cano, D. Banham, S.Y. Ye, A. Hintennach, J. Lu, M. Fowler, Z.W. Chen, *Nature Energy* 3 (2018) 279–289.
- [11] H. M. Song, C. Zuo, X. Q. Xu, Y. X. Wan, L. J. Wang, D. S. Zhou, Z.J. Chen, *RSC Adv.* 8 429–434.
- [12] L.H. Wang, Y.B. He, L. Shen, D.N. Lei, J.M. Ma, H. Ye, K. Shi, B.H. Li, F.Y. Kuang, *Nano Energy* 50 (2018) 367–375.
- [13] X.W. Wang, C.H. Yang, X.H. Xiong, G.L. Chen, M.Z. Huang, J.-H. Wang, Y. Liu, M.L. Liu, K. Huang, *Energy Storage Materials* 16 (2019) 344.
- [14] G.R. Li, S. Wang, Y.N. Zhang, M. Li, Z.C. Chen, J. Lu, *Adv. Mater.* 30 (2018) 1705590.
- [15] L. Kong, C. Yan, J.-Q. Huang, M.-Q. Zhao, M.-M. Titirici, R. Xiang, Q. Zhang, *Energy Environ. Mater.* 1 (2018) 100–112.
- [16] Y.J. Li, J.M. Fan, M.S. Zheng, Q.F. Dong, *Energy Environ. Sci.* 9 (2016) 1998–2004.
- [17] D.Z. Yang, L. He, Y. Liu, W.Q. Yan, S.S. Liang, Y.S. Zhu, L.J. Fu, Y.H. Chen, Y.P. Wu, *J. Mater. Chem. A* 7 (2019) 13679–13686.
- [18] Z.Z. Du, X.J. Chen, W. Hu, C.H. Chuang, S. Xie, A.J. Hu, W.S. Yan, X.H. Kong, X.J. Wu, H.X. Ji, L.J. Wan, *J. Am. Chem. Soc.* 141 (2019) 3977–3985.
- [19] Y. Jiang, Y.P. Deng, R.L. Liang, J. Fu, D. Luo, G.H. Liu, J.D. Li, Z.Y.F. Hu, Z.W. Chen, *Adv. Energy Mater.* (2019) 1900911.
- [20] J.S. Meng, C.J. Niu, L.H. Xu, J.T. Li, X. Liu, X.P. Wang, Y.Z. Wu, X.M. Xu, W.Y. Chen, Q. Li, Z.Z. Zhu, D.Y. Zhao, L.Q. Mai, *J. Am. Chem. Soc.* 139 (2017) 8212–8221.
- [21] J.T. Zhang, H. Hu, Z. Li, X.W. Lou, *Angew. Chem. Int. Ed.* 128 (2016) 4050–4054.
- [22] G.R. Li, W. Lei, D. Luo, Y.P. Deng, D.L. Wang, A.P. Yu, Z.C. Chen, *Energy Environ. Sci.* 11 (2018) 2372–2381.
- [23] J.T. Zhang, Z. Li, Y. Chen, S.Y. Gao, X.W. Lou, *Angew. Chem. Int. Ed.* 130 (2018)

- 11110–11114.
- [24] J.C. Acomb, C.F. Wu, P.T. Williams, *Appl. Catal. B Environ.* 180 (2016) 497–510.
- [25] Y.Z. Zhang, Z. Zhang, S. Liu, G.R. Li, X.P. Gao, *ACS Appl. Mater. Interfaces* 10 (2018) 8749–8757.
- [26] G.G. Kumar, S.H. Chuang, T.R. Kumar, A. Manthiram, *ACS Appl. Mater. Interfaces* 10 (2018) 20627–20634.
- [27] J.H. Kim, C. Young, J. Lee, Y.U. Heo, M.S. Park, M.S.A. Hossain, Y. Yamauchi, J.H. Kim, *J. Mater. Chem. A* 5 (2017) 15065–15072.
- [28] M. Sun, D. Davenport, H.J. Liu, J.H. Q. M. Elimelech, J.H. Li, *J. Mater. Chem. A* 6 (2018) 2527–2539.
- [29] D.L. Fang, Y.L. Wang, X.Z. Liu, J. Yu, C. Qian, S.M. Chen, X. Wang, S.J. Zhang, *ACS Nano* 13 (2019) 1563–1573.
- [30] S.Z. Wang, J.X. Liao, X.F. Yang, J.M. Liang, Q. Sun, J.W. Liang, F.P. Zhao, A. Koo, F.P. Kong, Y. Yao, X.J. Gao, M.Q. Wu, A.Z. Yang, X.L. Sun, *Nano Energy* 57 (2019) 230–240.
- [31] W. Chen, T.Y. Lei, W.Q. Lv, Y. Hu, Y.C. Yan, Y. Jiao, W.D. He, Z.H. Li, C.L. Yan, J. Xiong, *Adv. Mater.* 30 (2018) 1804084.
- [32] H.L. Wu, Y. Li, J. Ren, D.W. Rao, Q.J. Zheng, L. Zhou, D.M. Lin, *Nano Energy* 55 (2019) 82–92.
- [33] D. Luo, G.R. Li, Y.P. Deng, Z. Zhang, J.D. Li, R.L. Liang, M. Li, Y. Jiang, W.W. Zhang, Y.S. Liu, W. Lei, A.P. Yu, Z.W. Chen, *Adv. Energy Mater.* (2019) 1900228.
- [34] J.Q. Huang, X.L. Xu, S. Abouali, G.M. Garakani, J.M. Kim, *Carbon* 99 (2016) 624–632.
- [35] H.P. Li, L.C. Sun, Y. Zhao, T.Z. Tan, Y.G. Zhang, *Appl. Surf. Sci.* 466 (2019) 309–319.
- [36] F.Y. Fan, W.C. Carter, Y.M. Chiang, *Adv. Mater.* 27 (2015) 5203–5209.
- [37] L.C.H. Gerber, P.D. Frischmann, F.Y. Fan, S.E. Doris, X.H. Qu, A.M. Scheuermann, K. Persson, Y.M. Chiang, B.A. Helms, *Nano Lett.* 16 (2016) 549–554.
- [38] H.J. Peng, Z.W. Zhang, J.Q. Huang, G. Zhang, J. Xie, W.T. Xu, J.L. Shi, X. Chen, X.B. Cheng, Q. Zhang, *Adv. Mater.* 28 (2016) 9551–9558.
- [39] H.J. Peng, G. Zhang, X. Chen, Z.Z. Zhang, W.T. Xu, J.Q. Huang, Q. Zhang, *Angew. Chem. Int. Ed.* 55 (2016) 12990–12995.
- [40] S.F. Wang, X.H. Hou, Z.M. Zhong, K.X. Shen, G.Z. Zhang, L.M. Yao, F.M. Chen, *Sci. Rep.* 8 (2018) 16133.